Metallic Mo, Ru coupled with graphitic carbon dots to activate inertness 1D copper-based nanowires as efficient electrocatalyst for pH-universal hydrogen evolution reaction

Yingxue Du [a], Qichang Li [a], Linping Han [a], Pengfei Yang [d], Liantao Xin [a], Wei Jin [b], Weiping Xiao [c], Zhenjiang Li [e], Jinsong Wang [f], Zexing Wu [a,*], Lei Wang [a,*]

[a] *Key Laboratory of Eco-chemical Engineering, Ministry of Education, International Science and Technology Cooperation Base of Eco-chemical Engineering and Green Manufacturing, College of Chemistry and Molecular Engineering, Qingdao University of Science & Technology, 53 Zhengzhou Road, 266042 Qingdao, PR China*
[b] *School of Environmental Science and Engineering, Suzhou University of Science and Technology, Suzhou 215009, PR China*
[c] *College of Science, Nanjing Forestry University, Nanjing 210037, PR China*
[d] *College of Chemical Engineering, Qingdao University of Science and Technology, Qingdao 266042, PR China*
[e] *College of Materials Science and Engineering, Key Laboratory of Polymer Material Advanced Manufacturing's Technology of Shandong Province, Qingdao University of Science & Technology, 53 Zhengzhou Road, 266042 Qingdao, PR China*
[f] *Faculty of Materials Science and Engineering, Kunming University of Science and Technology, Kunming 650093, PR China*

ARTICLE INFO

ABSTRACT

Designing efficient and robust pH-universal electrocatalysts for hydrogen evolution reaction (HER) is the key to boost the development of eco-friendly hydrogen energy. Herein, metallic Mo, Ru coupled with graphitic carbon dots (GQDs) activate inertness 1D copper-based nanowires (GQDs@ Ru, Mo-Cu$_2$O/CF) by surface chemical oxidation, solvothermal and low temperature calcination. The metals of Mo, Ru favor the water-dissociation and optimize the hydrogen adsorption/desorption. In addition, GQDs owns edge effect and good conductivity, and then benefiting electron transport and active sites exposure. Therefore, the synthesized GQDs@ Ru, Mo-Cu$_2$O/CF requires only 30, 39, 17 and 55 mV in alkaline, acidic, alkaline seawater and neutral to achieve 10 mA cm^{-2}. Moreover, the assembled electrolyzer requires 1.58 V to reach 10 mA cm^{-2} in alkaline seawater, and maintained well at 200 mA cm^{-2} for 100 h. This research opens a new avenue for designing efficient catalysts on energy-relation applications through introducing both metal and non-metal.

1. Introduction

In order to achieve the goal of carbon neutrality, it is particularly important to develop alternatives to traditional fossil fuels [1,2]. Hydrogen energy has attracting widespread attention as regards its high-energy density and its green properties [3–6]. Electrocatalytic is an efficient way to produce hydrogen without greenhouse gases generation [7,8]. However, the slowly occurring kinetics of the hydrogen evolution reaction (HER) limits the catalytic productivity of water electrolysis [9–13]. Therefore, it is necessary to develop highly-efficient electro-catalysts to decrease the energy barrier to expedite hydrogen production. Until now, platinum (Pt) and its derivatives are considered as the most favorable catalysts for HER [14–18]. However, low Pt reserves lead to high costs and then limiting its commercial application. Relatively, the metal Ru is only 1/4 of the cost of Pt, but has a Pt-H-like bond and

comparable catalytic activity to Pt [19,20]. Thus, it is promising to design efficient electrocatalysts with low ruthenium content.

Copper-based materials have attracted much attentions as low-cost and reserve-rich transition metal on various energy-related reactions [21,22]. In particular, copper foam (CF), as self-supported three-dimensional (3D) foam, can avoid the usage of binders and enlarge the area of contact between the catalyst and the electrolyte [23,24]. Therefore, it is often investigated as substrate to synthesize efficient electrocatalysts [25,26]. Generally, copper-based compounds exhibit inert catalytic performance for HER, and then it is of importance to develop valid approaches to boost the reaction kinetics [27–29]. Among them, tuning the electronic structure of transition metal-based catalysts by doping with heteroatom is a viable method to improve the catalyst performance by optimizing the reaction energy barriers and accelerating the reaction kinetics [30–32]. In addition, heteroatom doping not only

---

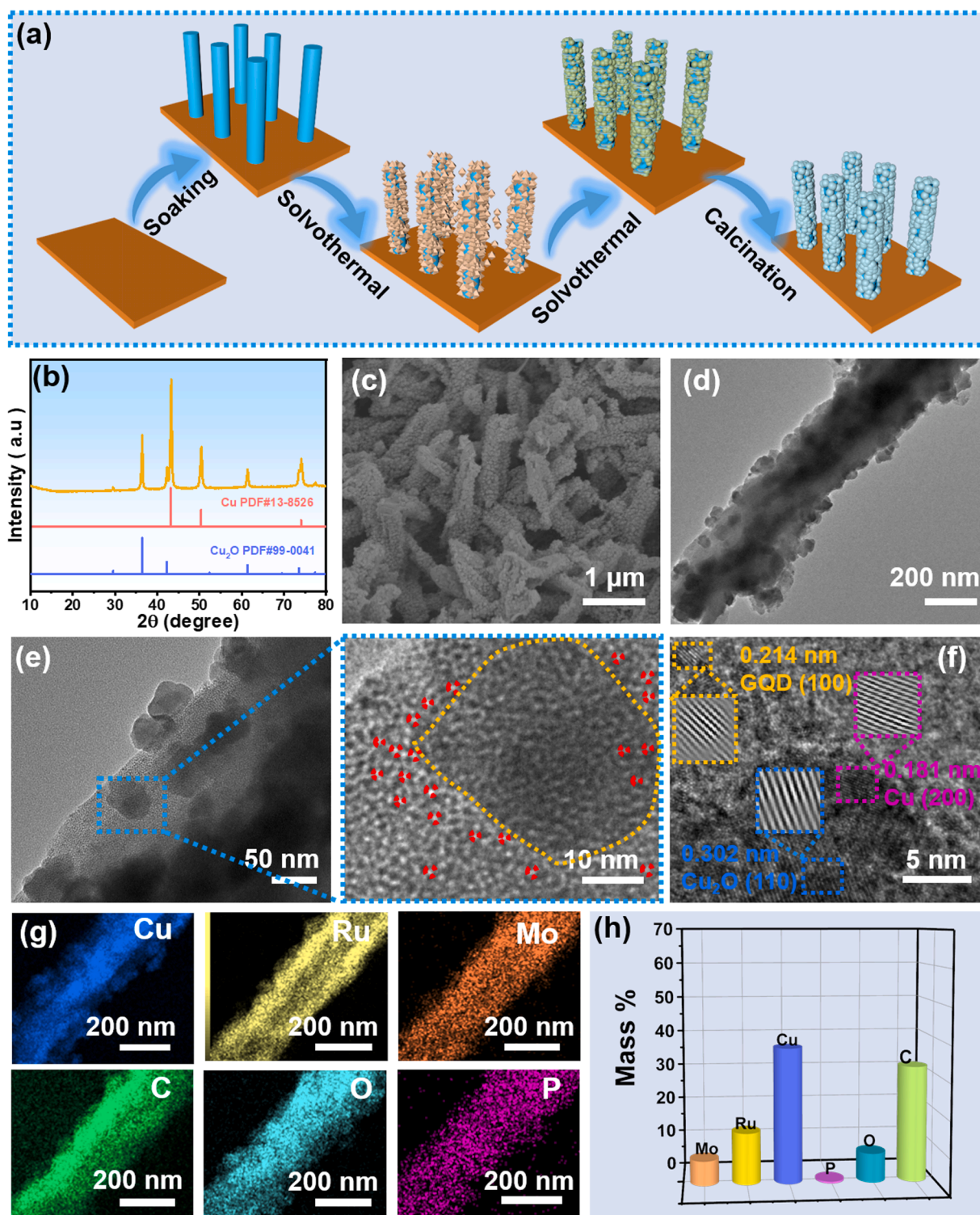**Fig. 1.** (a) Schematic diagram of the synthesis of GQDs@ Ru, Mo-Cu$_2$O/CF. (b) XRD pattern, (c) SEM, (d) TEM and (e) local detail TEM images of GQDs@ Ru, Mo-Cu$_2$O/CF. (f) HR-TEM, (g) EDX mappings and (h) atomic analysis of GQDs@ Ru, Mo-Cu$_2$O/CF.

changes the surface morphology, but also increases the number of active sites and facilitate mass/electron transfer during the catalytic process, thereby improving the electrocatalytic activity [33]. For example, Xue et al. reported that the electrocatalytic performance of CoS$_2$ nanowire improved efficiently via Mn doping, this is due to the fact that Mn can act as a new active site in the CoS$_2$ matrix [34]. As a typical 0-dimensional material, graphene quantum dots (GQDs) have received a great deal of attentions owing to its excellent edge effects and quantum

confinement [35–37]. GQDs are capable of facilitating charge transfer and transport that occurs at interfaces with electrolytes or other nano-materials and is mediated by localized active portions or sp^2 carbon structural domains [38]. However, the synthesis steps of GQDs are complex and environmental unfriendly, and the tunable control of GQDs deposition remains unsatisfactory [39]. Therefore, designing simple methods to synthesize GQDs-doped nanomaterials is expected to achieve robust and efficient hydrogen production from the catalysts.
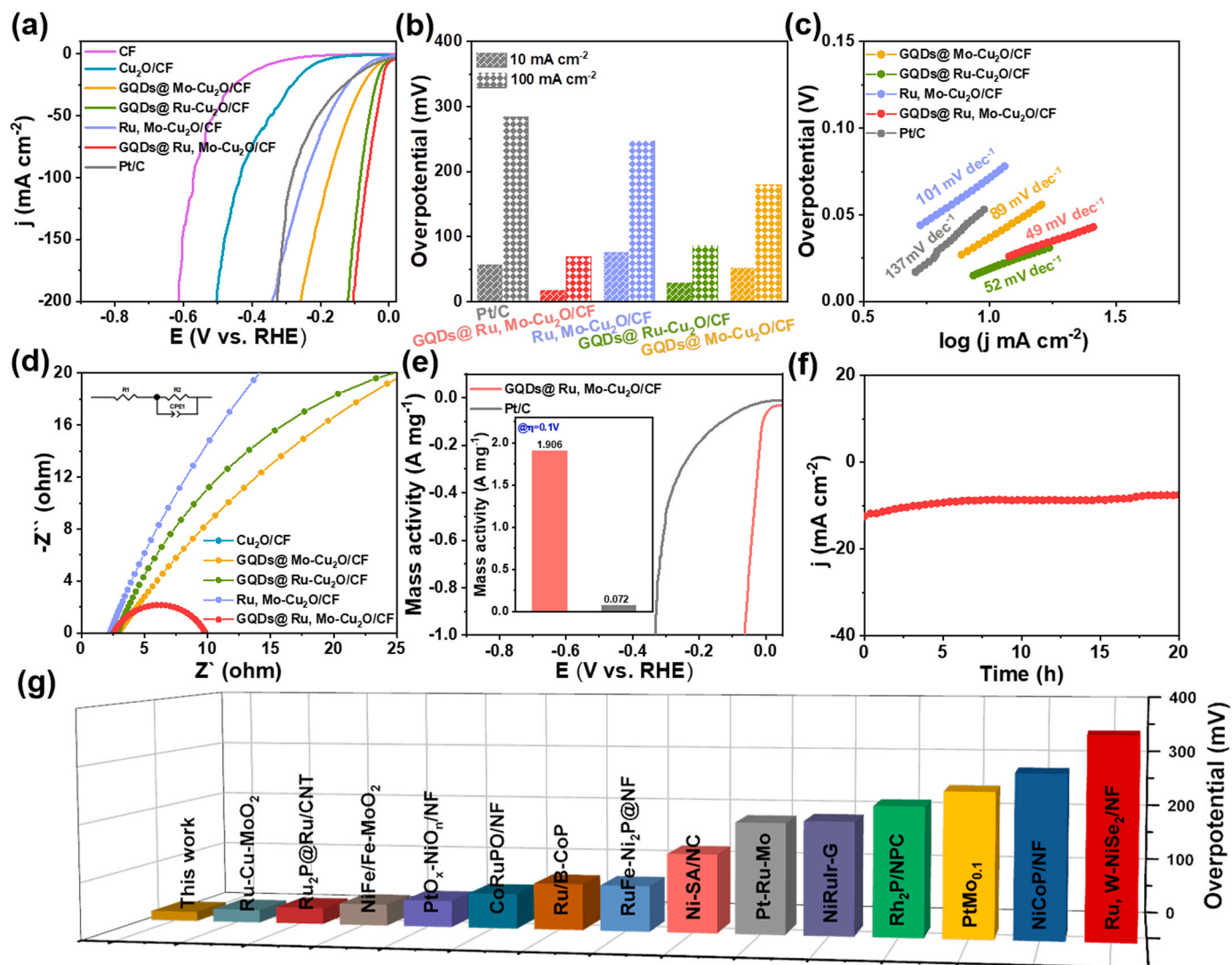
Fig. 5. Electrochemical measurement of catalysts in 1 M KOH+ seawater. (a) The HER polarizations of GQDs@ Ru, Mo-Cu$_2$O/CF, Ru, Mo-Cu$_2$O/CF, GQDs@ Ru-Cu$_2$O/CF, GQDs@ Mo-Cu$_2$O/CF, Cu$_2$O/CF and Pt/C. (b) Comparison of the overpotentials of electrocatalysts. (c) Tafel slopes. (d) Nyquist plots. (e) Polarization curves after normalization for precious metal content (Inset: Mass activity comparison of GQDs@ Ru, Mo-Cu$_2$O/CF and Pt/C). (f) Long-term chronoamperometric of GQDs@ Ru, Mo-Cu$_2$O/CF in 1 M KOH+ seawater. (g) Compared of HER performance of GQDs@ Ru, Mo-Cu$_2$O/CF with reported precious metal-based electrocatalysts.

In this work, a simple and valid approach is applied to activate inert 1D copper-based nanowires (GQDs@ Ru, Mo-Cu$_2$O/CF) by introducing Mo, Ru and GQDs. The Mo and Ru can not only interact with metal copper, but also a key factor in accelerating the reaction kinetics. In addition, GQDs are uniformly dispersed in the nanowire, which can accelerate the electron transfer and expose abundant active sites. Furthermore, the specific 1D nanowire morphology with rich edge provides enriched active sites and favors the electrolyte transport. The in-situ synthesized electrocatalyst onto porous copper foam is also conducive the fast release of formed bubbles to expose the active sites timely. Thus, the prepared GQDs@ Ru, Mo-Cu$_2$O/CF achieves pH-universal hydrogen evolution and surpass most of the reported noble metal-containing electrocatalysts. Interestingly, the prepared GQDs@ Ru, Mo-Cu$_2$O/CF can utilize solar energy to drive water-splitting and then stored it into hydrogen energy.

2. Experimental

2.1. Materials

Ammonium persulfate ((NH_4)$_2$S$_2$O$_8$, Macklin), sodium hydroxide (NaOH, Aladdin), ruthenium trichloride hydrate (RuCl$_3$·xH$_2$O, Aladdin), phosphomolybdic acid hydrate (H$_3$PMo$_{12}$O$_{40}$·28H$_2$O, Aladdin), 2, 5-Dihydroxy terephthalic acid (DHTA, Aladdin), N, N-Dimethylformamide (DMF, Macklin).

2.2. Samples synthesis

2.2.1. Synthesis of Cu(OH)$_2$/CF

At room temperature, 3.2 g NaOH and 1 g (NH_4)$_2$S$_2$O$_8$ are dissolved into 40 mL of deionized water. Then, 6 sheets of CF (1 *1.5 cm^2) are placed into the above solution for 20 min. Finally, the copper foam (CF) is rinsed several times with deionized water and dried at 60 °C overnight to obtain Cu(OH)$_2$ nanowires on CF (Cu(OH)$_2$/CF).
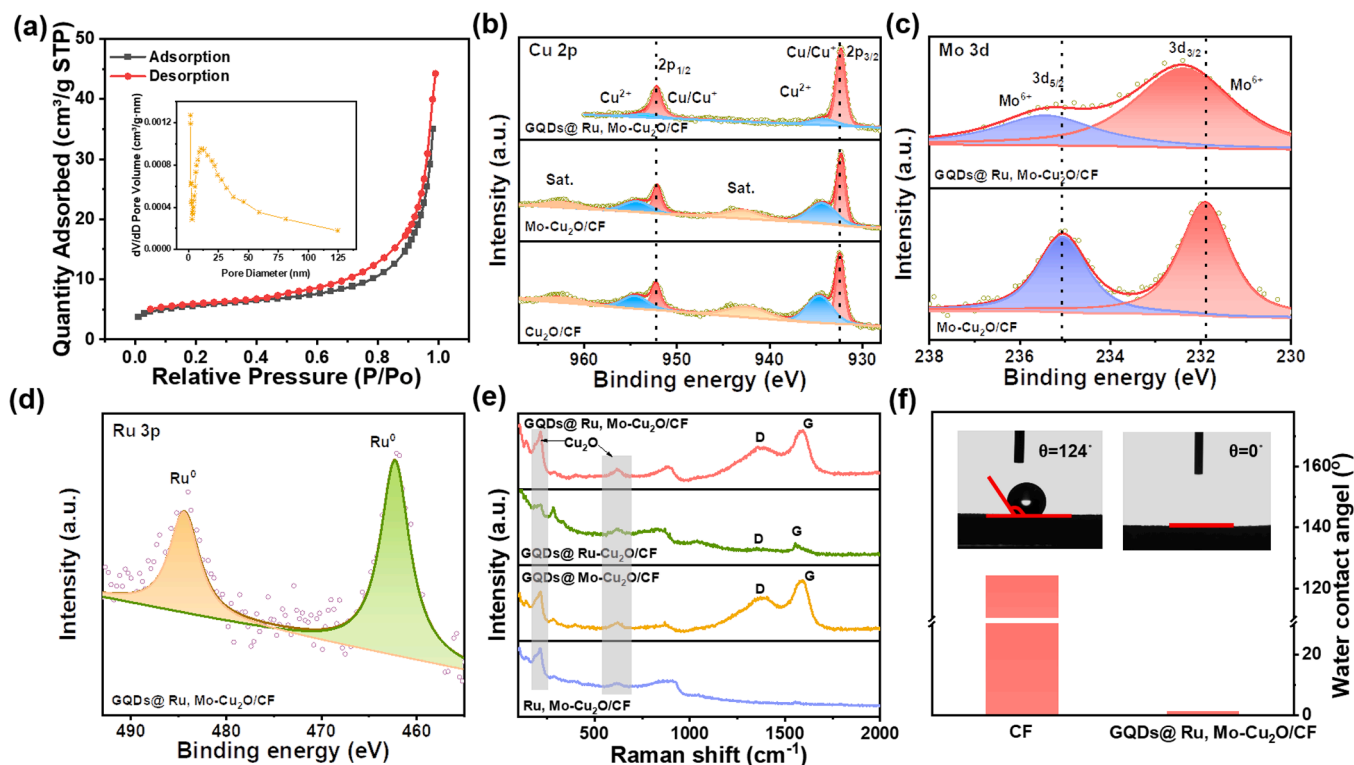
Fig. 2. (a) N_2 adsorption/desorption isotherm curves of GQDs@ Ru, Mo-Cu$_2$O/CF. XPS spectra of Cu 2p (b), Mo 3d (c) and Ru 3p. (e) Raman spectra of GQDs@ Ru, Mo-Cu$_2$O/CF, GQDs@ Ru- Cu$_2$O/CF and GQDs@ Mo- Cu$_2$O/CF, Ru, Mo- Cu$_2$O/CF. (f) Contact angle tests of CF and GQDs@ Ru, Mo- Cu$_2$O/CF.

2.2.2. Synthesis of Mo-Cu(OH)$_2$/CF

0.1 g of $H_3PMo_{12}O_{40}\cdot28H_2O$ was dissolved in deionized water (30 mL), and then transferred to a Teflon reactor with two pieces of Cu (OH)$_2$/CF. Then, it reacted at 120 °C for 12 h to achieve Mo-Cu(OH)$_2$/CF.

2.2.3. Synthesis of Ru, Mo-Cu(OH)$_2$/CF/C

0.1 g 2, 5- Dihydroxy terephthalic acid (DHTA) and 10 mg RuCl$_3\cdot$xH$_2$O were dissolved in DMF (30 mL) and subsequently transferred to a Teflon reactor and put into two pieces of Mo-Cu(OH)$_2$/CF and reacted at 120 °C for 12 h.

2.2.4. Synthesis of GQDs@ Ru, Mo-Cu$_2$O/CF

The dried Ru, Mo-Cu(OH)$_2$/CF/C was calcined in a mixed gas of Ar (90 sccm) and H$_2$ (10 sccm) at 400 °C for two hours (ramp rate of 5 °C min^{-1}) to obtain GQDs@ Ru, Mo-Cu$_2$O/CF.

3. Results and discussion

Fig. 1a illustrates the preparation of GQDs@ Ru, Mo-Cu$_2$O/CF, in which copper foam (CF) with good conductivity and low cost is used as the substrate. 1D copper hydroxide nanowires (Fig. S1a-b) are first in-situ grown on the smooth CF (Fig. S2) surface by oxidative etching engineering. Then the cubic blocks are grown on Cu(OH)$_2$ nanowires by solvothermal (Fig. S3). After that, Ru is dispersed on the nanowires via solvothermal with DHTA. Scanning electron microscopy (SEM) and transmission electron microscopy (TEM) results show that the nanowires are loaded with nanoparticles on the surface and coated by the ligand layer. (Figs. S4, 5). Finally, GQDs@ Ru, Mo-Cu$_2$O/CF is obtained by calcination treatment. In order to investigate the components of GQDs@ Ru, Mo-Cu$_2$O/CF, X-ray diffraction (XRD) test is performed (Fig. 1b). It reveals that GQDs@ Ru, Mo-Cu$_2$O/CF is consisted of Cu (PDF#13–8526) and Cu$_2$O (PDF#99–0041) [40]. The nanowire structure with uniformly nanoparticles on the surface is clearly observed by SEM in Fig. 1c. It is noteworthy that the uniformed nanoparticle

facilitates the contact between the electrode and the electrolyte, and then can shorten the ionic reaction path to accelerate the reaction process [41]. TEM image further verifies the microstructure of GQDs@ Ru, Mo-Cu$_2$O/CF as nanowires with surface-loaded nanoparticles (Fig. 1d). In addition, GQDs with diameter of about 1 nm are observed in Fig. 1e (red dotted circle). The lattice spacings of 0.214, 0.181 and 0.302 nm in the high-resolution TEM (HR-TEM) image (Fig. 1f) are corresponded to (100), (200) and (110) crystal planes of GQDs, Cu and Cu$_2$O, respectively [42–44]. The EDX mappings represent the well-spread of Cu, Ru, Mo, C, O and P (Fig. 1g), and the contents of each atom are illustrated in Fig. 1h. In addition, line scan test of nanoparticle on nanowires is shown in Fig. S6, demonstrating the nanoparticle is mainly composed by Cu. The Ru content is measured by inductively coupled plasma (ICP) to be about 0.8461 *wt*%.

The nitrogen adsorption/desorption isotherm demonstrates that GQDs@ Ru, Mo-Cu$_2$O/CF has the largest surface area of 18.31 m^2/g with mesoporous structure compared with GQDs@ Ru- Cu$_2$O/CF (4.37 m^2/g), GQDs@ Mo- Cu$_2$O/CF (1.66 m^2/g) and Ru, Mo- Cu$_2$O/CF (5.29 m^2/g). (Fig. 2a and Fig. S7a-d). X-ray photoelectron spectroscopy (XPS) is used to study the chemical valence of GQDs@ Ru, Mo-Cu$_2$O/CF. The total XPS spectrum verifies the presence of Cu, Mo, Ru, C, O and P elements (Fig. S8). For the spectrum of Cu 2p (Fig. 2b), two sets of peaks can be observed, with peaks at 952.5 and 932.7 eV ascribed to Cu/Cu$^+$, verifying the presence of Cu and Cu$_2$O in GQDs@ Ru, Mo-Cu$_2$O/CF [45–47]. The unavoidable exposure of the sample to air leads to its slight oxidation or its incomplete reduction, resulting in the generation of Cu^{2+} (934.2 and 954.1 eV) [48]. By comparison, it is found that there is no significant shift in the binding energy after the introduction of the metals Mo, Ru indicating a stable state. For Mo 3d (Fig. 2c), the peaks located at 232.3 and 235.4 eV are ascribed to Mo^{6+} [49]. The peaks situated at 462.3 and 484.4 eV, as shown in Fig. 2d, are identified as Ru^0 [50]. Relative to Mo-Cu$_2$O/CF, the peaks in the Mo 3d spectra of GQDs@ Ru, Mo-Cu$_2$O/CF are shifted to higher binding energies after the introduction of Ru, demonstrating that electronic interactions between Mo and Ru occurred [51]. For C 1 s + Ru 3d (Fig. S9a), the peaks at
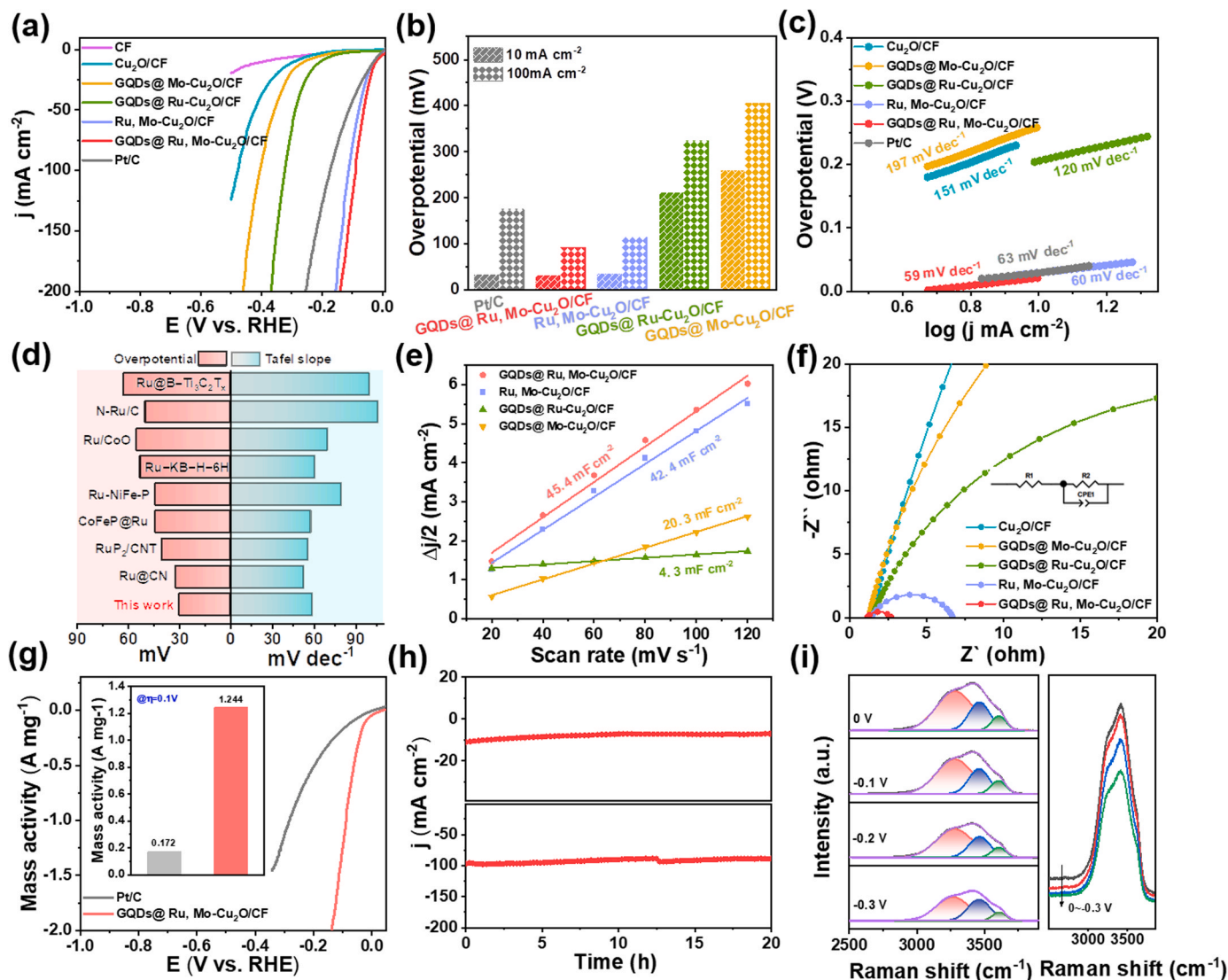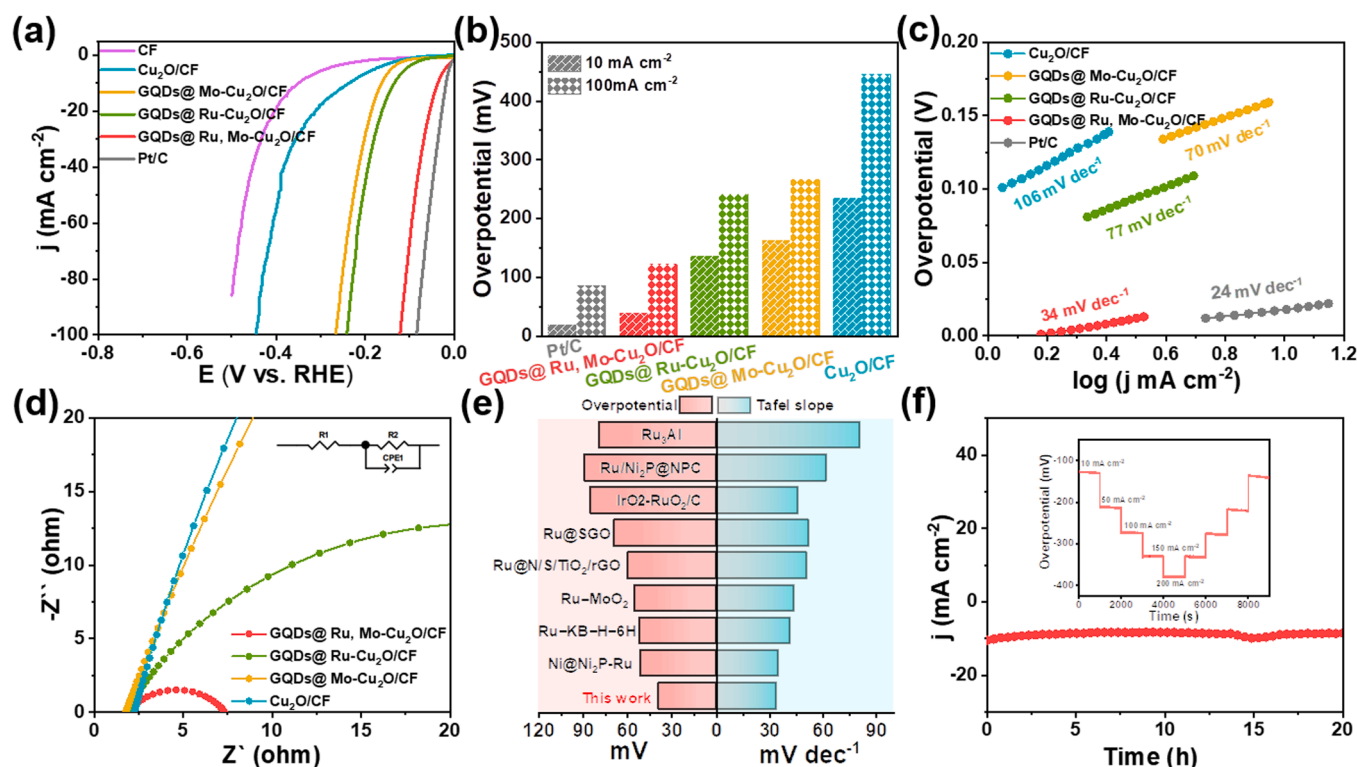
Fig. 3. Electrochemical measurement of catalysts in 1 M KOH. (a) HER curves of GQDs@ Ru, Mo-Cu$_2$O/CF, Ru, Mo- Cu$_2$O/CF, GQDs@ Ru-Cu$_2$O/CF and GQDs@ Mo-Cu$_2$O/CF, Cu$_2$O/CF and Pt/C. (b) Comparison of the overpotentials of electrocatalysts. (c) Tafel slopes. (d) Compared of HER performance of GQDs@ Ru, Mo-Cu$_2$O/CF with reported ruthenium-contained electrocatalysts. (e) The C$_{dl}$ of GQDs@ Ru, Mo-Cu$_2$O/CF and comparison samples. (f) Nyquist plots. (g) Polarization curves after normalization for precious metal content (Insert: Mass activity comparison of GQDs@ Ru, Mo-Cu$_2$O/CF and Pt/C). (h) Long-term chronoamperometric curve of GQDs@ Ru, Mo-Cu$_2$O/CF at low and high current densities. (i) In-situ Raman spectra of GQDs@ Ru, Mo-Cu$_2$O/CF.

280.5 eV is corresponded to mental Ru [52], and the peaks at 284.7 and 286.3 eV are C-C/C═C and C-OH [53,54]. The peaks in O 1 s are assigned to M-O and C-O (Fig. S9b) [55–57]. For P 2p (Fig. S9c), only one group of peaks are detected for P^{5+} [58]. The Raman spectra of GQDs@ Ru, Mo-Cu$_2$O/CF and its comparison samples are showing in Fig. 2e, the peaks at 1360 cm^{-1} and 1580 cm^{-1} are attributed to the D and G of carbon, demonstrating the existence of C [59]. The peaks at 216 cm^{-1}, and 400–500 cm^{-1} are attributed to the presence of Cu$_2$O [60,61]. Remarkably, the contact angle of water for CF is 124° (Fig. 2f), and it is reduced to 0° of treated GQDs@ Ru, Mo-Cu$_2$O/CF, indicating its superhydrophilicity property and then facilitating the contact between electrode and electrolyte to accelerate the reaction kinetics [62].

A standard three-electrode system is used to study electrochemical performance of all the samples. In 1 M KOH electrolyte, the untreated copper foam has almost no activity, while the prepared GQDs@ Ru, Mo-Cu$_2$O/CF shows the best electrochemical performance, even exceeding Pt/C (Fig. 3a and Fig. S10). According to Fig. 3b, GQDs@ Ru, Mo-Cu$_2$O/ CF only needs 30 and 92 mV to reach 10 and 100 mA cm^{-2}, lower than Pt/C (33, 175 mV), Ru, Mo-Cu$_2$O/CF (35, 114 mV), GQDs@ Ru-Cu$_2$O/

CF (211, 323 mV) and GQDs@ Mo-Cu$_2$O/CF (259, 405 mV), demonstrating the introduction of metallic Mo, Ru and nonmetallic GQDs effectively improves the catalytic activity. Tafel slopes are obtained based on LSV curves to compare the reaction kinetic (Fig. 3c). Among them, the Tafel of GQDs@ Ru, Mo-Cu$_2$O/CF is 59 mV dec^{-1}, which is smaller than Pt/C (63 mV dec^{-1}), Ru, Mo-Cu$_2$O/CF (60 mV dec^{-1}), GQDs@ Ru-Cu$_2$O/CF (120 mV dec^{-1}) and GQDs@ Mo-Cu$_2$O/CF (197 mV dec^{-1}), verifying the incorporation of GODs and Mo, Ru plays a key role in boosting the reaction kinetics. Remarkably, GQDs@ Ru, Mo-Cu$_2$O/CF exhibits excellent electrochemical activity in 1 M KOH compared to other reported Ru-based catalysts (Fig. 3d and Table S1). Cyclic voltammetry (CV) tests are performed at different scanning speeds to calculate the electrochemical double layer capacitance (C$_{dl}$) and then evaluate the electrocatalytic activity (Fig. 3e and Fig. S11). The prepared GQDs@ Ru, Mo-Cu$_2$O/CF has the largest C$_{dl}$ value of 45.4 mF cm^{-2} relative to the comparison samples, demonstrating its abundant exposure active sites [63]. As shown in Fig. 3f, GQDs@ Ru, Mo-Cu$_2$O/CF exhibits the smallest arc, indicating the quickest charge transfer at the electrode and electrolyte interface. In addition, GQDs@ Ru,
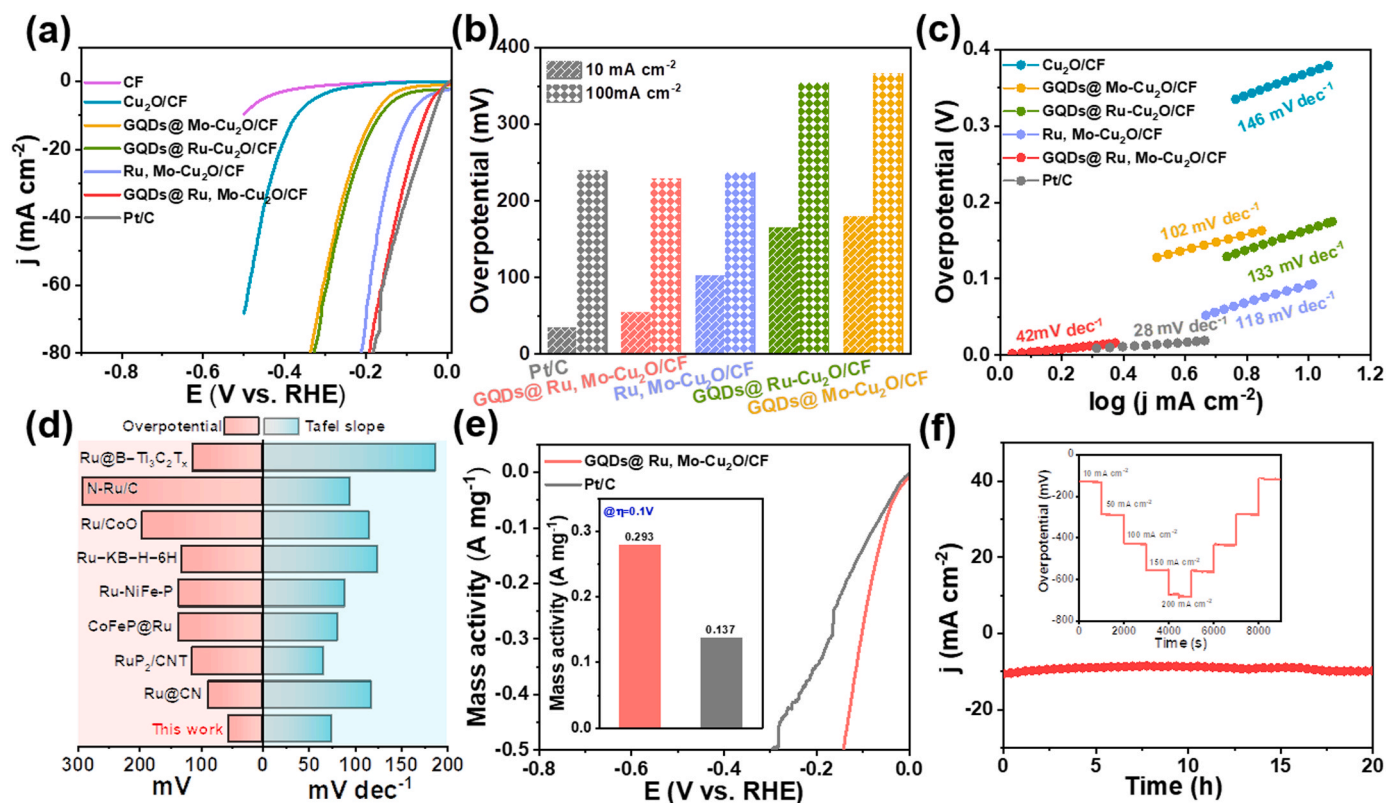
Fig. 4. Electrochemical measurement of catalysts in 0.5 M H_2SO_4. (a) HER curves of GQDs@ Ru, Mo-Cu$_2$O/CF, GQDs@ Ru-Cu$_2$O/CF, GQDs@ Mo-Cu$_2$O/CF, Cu$_2$O/CF and Pt/C. (b) Comparison of the overpotentials of electrocatalysts. (c) Tafel slopes. (d) Nyquist plots. (e) Compared of HER performance of GQDs@ Ru, Mo-Cu$_2$O/CF with reported ruthenium-contained electrocatalysts. (f) Long-term chronoamperometric of GQDs@ Ru, Mo-Cu$_2$O/CF in 0.5 M H_2SO_4 (Inset: the multi-step chronopotentiometric curve of GQDs@ Ru, Mo-Cu$_2$O/CF).

Mo-Cu$_2$O/CF has a mass activity of 1.244 A mg^{-1} at the potential of − 0.1 V, which is about seven times to that of Pt/C (Fig. 3g and inset). For electrocatalysis, the preferred value for comparing the intrinsic activity of catalysts is turn-over frequency (TOF). As shown in Fig. S12, the highest TOF per surface site for GQDs@ Ru, Mo-Cu$_2$O/CF is 0.407 H$_2$ s^{-1} at − 0.1 V, while the TOFs for Ru, Mo-Cu/Cu$_2$O/CF, GQDs@ Ru-Cu/Cu$_2$O/CF and GQDs@ Mo-Cu/Cu$_2$O/CF are 0.202, 0.030 and 0.008 H$_2$ s^{-1}, respectively, indicating GQDs@ Ru, Mo-Cu$_2$O/CF produces the largest amount of hydrogen molecules per second at each surface site. The multi-step chronopotentiometric and long-term chronoamperometric test are performed to verify its robustness and reversibility. (Fig. 3h and Fig. S13). And then, LSV (uncompensated) curves of GQDs@ Ru, Mo-Cu$_2$O/CF before and after stabilization shows no significant decline, and the stabilized SEM exhibits no apparent change, further indicating excellent stability (Fig. S14a, b). Moreover, there are no significant change of the chemical composition and elemental valence in GQDs@ Ru, Mo-Cu$_2$O/CF after low and high current densities stability test, demonstrating its strong structure (Fig. S15) [64]. The dynamics of the hydrogen evolution process of GQDs@ Ru, Mo-Cu$_2$O/CF in 1 M KOH was confirmed by in-situ Raman spectroscopy. As illustrated in Fig. 3i, the peaks of interfacial water can be divided into three peaks, and the peaks located at ~3225 cm^{-1} and ~3450 cm^{-1} are corresponded to tetrahedral and trihedral coordination water at the interface, respectively, while the peak located at ~3615 cm^{-1} is corresponded to the interfacial inactive water molecules with dangling O-H bond [65,66]. Furthermore, the peak intensity of the dangling O-H bond of interfacial water decreases with decreasing potential, indicating water is effectively dissociated at the GQDs@ Ru, Mo-Cu$_2$O/CF surface [66,67].

Electrochemical testing of GQDs@ Ru, Mo-Cu$_2$O/CF and its contrast samples in 0.5 M H_2SO_4 were also studied. As shown in Fig. 4a, b and Fig. S16, the overpotential of GQDs@ Ru, Mo-Cu$_2$O/CF at 10 mA cm^{-2} is only 39 mV, closing to Pt/C (19 mV), and lower than GQDs@ Ru-

Cu$_2$O/CF (135 mV), GQDs@ Mo-Cu$_2$O/CF (163 mV) and Cu$_2$O/CF (235 mV). Furthermore, the overpotential (122 mV) of GQDs@ Ru, Mo-Cu$_2$O/CF at 100 mA cm^{-2} is also lower than its comparison samples. GQDs@ Ru, Mo-Cu$_2$O/CF also has the smallest Tafel slope of 34 mV dec^{-1} (Fig. 4c) compare with GQDs@ Ru-Cu$_2$O/CF (77 mV dec^{-1}), GQDs@ Mo-Cu$_2$O/CF (70 mV dec^{-1}), and Cu$_2$O/CF (106 mV dec^{-1}), demonstrating the favorable reaction kinetics of GQDs@ Ru, Mo-Cu$_2$O/CF. In addition, EIS testing further verifies that GQDs@ Ru, Mo-Cu$_2$O/CF has optimal reaction kinetics (Fig. 4d). The synthesized GQDs@ Ru, Mo-Cu$_2$O/CF exhibits smaller overpotential and Tafel slope compare with the previously reported Ru-based electrocatalytic materials (Fig. 4e and Table S2). As shown in the Fig. S17 and inset, the mass activity of GQDs@ Ru, Mo-Cu$_2$O/CF (0.683 A mg^{-1} at η = 100 mV) is significantly higher than that of Pt/C (0.499 A mg^{-1} at η = 100 mV). Moreover, GQDs@ Ru, Mo-Cu$_2$O/CF has the highest TOF value compared to the reference samples, with a TOF value of 0.055 H$_2$ s^{-1} at overpotential of 100 mV (Fig. S18), indicating GQDs@ Ru, Mo-Cu$_2$O/CF produces the largest amount of hydrogen molecules per second at each surface site. Besides, the long-term stability test and multi-step chronopotentiometric test show good stability, indicating that GQDs@ Ru, Mo-Cu$_2$O/CF has robust mechanical properties (Fig. 4f and inset).

Due to the scarcity of fresh water resources, direct electrolysis of seawater to produce hydrogen is considered as a promising strategy. Alkaline natural seawater electrolyte is prepared for HER testing of GQDs@ Ru, Mo-Cu$_2$O/CF and comparison samples. GQDs@ Ru, Mo-Cu$_2$O/CF exhibits better HER performance relative to the studied samples (Fig. 5a and Fig. S19). GQDs@ Ru, Mo-Cu$_2$O/CF only requires 17 and 69 mV to reach 10 and 100 mA cm^{-2}, lower than Pt/C (57, 284 mV), Ru, Mo-Cu$_2$O/CF (76, 247 mV), GQDs@ Ru-Cu$_2$O/CF (29, 86 mV) and GQDs@ Mo-Cu$_2$O/CF (51, 180 mV) (Fig. 5b). Fig. 5c shows the Tafel slopes of GQDs@ Ru, Mo-Cu$_2$O/CF and its comparison samples. GQDs@ Ru, Mo-Cu$_2$O/CF has the lowest Tafel slope is 49 mV dec^{-1}, indicating its excellent reaction kinetics. In the other hand,

Fig. 6. Electrochemical measurement of catalysts in 1 M PBS. (a) The HER polarizations of GQDs@ Ru, Mo-Cu$_2$O/CF, Ru, Mo-Cu$_2$O/CF, GQDs@ Ru-Cu$_2$O/CF, GQDs@ Mo-Cu$_2$O/CF, Cu$_2$O/CF and Pt/C. (b) Comparison of the overpotentials of electrocatalysts. (c) Tafel slopes. (d) Compared of HER performance of GQDs@ Ru, Mo-Cu$_2$O/CF with reported ruthenium-contained electrocatalysts. (e) Polarization curves after normalization for precious metal content (Insert: Mass activity comparison of GQDs@ Ru, Mo-Cu$_2$O/CF and Pt/C). (f) Long-term chronoamperometric of GQDs@ Ru, Mo-Cu$_2$O/CF in 1 M PBS (Inset: the multi-step chronopotentiometric curve of GQDs@ Ru, Mo-Cu$_2$O/CF).

GQDs@ Ru, Mo-Cu$_2$O/CF has the smallest semicircular arc, further verifying its good reaction kinetics (Fig. 5d). Fig. 5e and inset shown the mass activity of GQDs@ Ru, Mo-Cu$_2$O/CF (1.906 A mg^{-1} at $\eta = 100$ mV) is significantly higher than that of Pt/C (0.072 A mg^{-1} at $\eta = 100$ mV). Moreover, GQDs@ Ru, Mo-Cu$_2$O/CF shows almost no decline of activity and no deposits on the CF after a long-term stability test of 20 h (Fig. 5f). In addition, the synthesized GQDs@ Ru, Mo-Cu$_2$O/CF exhibits smaller overpotential than recently reported precious metal-based electrocatalysts. (Fig. 5g and Table S3).

The HER activity of GQDs@ Ru, Mo-Cu$_2$O/CF and its comparison samples is compared in 1 M PBS. Fig. 6a-b and Fig. S20 show GQDs@ Ru, Mo-Cu$_2$O/CF only needs 55 and 229 mV to reach 10 and 100 mA cm^{-2}, which is lower than Ru, Mo-Cu$_2$O/CF (102, 237 mV), GQDs@ Ru -Cu$_2$O/CF (165, 354 mV) and GQDs@ Mo-Cu$_2$O/CF (180, 366 mV). The Tafel slope of the GQDs@ Ru, Mo-Cu$_2$O/CF is 42 mV dec^{-1} (Fig. 6c), which is clearly lower than Ru, Mo-Cu$_2$O/CF (118 mV dec^{-1}), GQDs@ Ru-Cu$_2$O/CF (133 mV dec^{-1}), and GQDs@ Mo-Cu$_2$O/CF (102 mV dec^{-1}), demonstrating the reaction kinetics of GQDs@ Ru, Mo-Cu$_2$O/CF is better than other samples, and the EIS further indicates its excellent reaction kinetics (Fig. S21). In addition, the synthesized GQDs@ Ru, Mo-Cu$_2$O/CF exhibits smaller overpotential and Tafel slope compared to the previously reported Ru-based electrocatalytic materials (Fig. 6d and Table S4). Fig. 6e shows the mass activity of GQDs@ Ru, Mo-Cu$_2$O/CF (0.293 A mg^{-1} @100 mV) is larger than that of Pt/C (0.137 A mg^{-1} @100 mV), (Fig. 6e). As shown in Fig. S22, GQDs@ Ru, Mo-Cu$_2$O/CF has the highest TOF value compared to the comparison sample, with a TOF value of 0.091 H$_2$ s^{-1} at 100 mV, demonstrating GQDs@ Ru, Mo-Cu$_2$O/CF produces the highest amount of hydrogen molecules per second at each surface site [68]. More importantly, the prepared GQDs@ Ru, Mo-Cu$_2$O/CF possesses excellent reversibility and

stability. It can return to the initial potential after a reversible process, and present negligible current density loss for 20 h (Fig. 6f and inset).

Owing to the excellent HER activity of GQDs@ Ru, Mo-Cu$_2$O/CF in alkaline and alkaline seawater. Therefore, a two-electrode system with GQDs@ Ru, Mo-Cu$_2$O/CF as the cathode and NiFe foam as the anode is established to investigate the water-splitting activity of GQDs@ Ru, Mo-Cu$_2$O/CF ‖ NiFe in alkaline and alkaline seawater. As displayed in Fig. 7a, b, the assembled electrolyzer exhibits good electrochemical activity of 1.60 V and 1.58 V in alkaline and alkaline seawater, even exceeding Pt/C ‖ RuO$_2$ (1.59 V and 1.63 V). In addition, long-term stability tests are performed in different electrolytes at 10 mA cm^{-2}. The multi-step chronopotentiometric testing of GQDs@ Ru, Mo-Cu$_2$O/CF proves its reversibility in 1 M KOH (Fig. 7c). In addition, GQDs@ Ru, Mo-Cu$_2$O/CF operates for 24 h at a low current density of 10 mA cm^{-2} in alkaline and alkaline seawater (Fig. S23). Moreover, the GQDs@ Ru, Mo-Cu$_2$O/CF maintains well for 100 h at 200 mA cm^{-2} in 1 KOH+ seawater, demonstrating its robust stability. (Fig. 7d). Obviously, the assembled electrolyzer exhibits comparable cell voltages with other reported values in both alkaline freshwater and seawater media, verifying its potential applications for hydrogen generation (Fig. 7e and Table S5). Based on the good electrochemical activity of GQDs@ Ru, Mo-Cu$_2$O/CF ‖ NiFe, the sustainable solar energy is used to drive the electrolyzer for continuous hydrogen production, and sumless bubbles generated on the electrode (Fig. 7f and Movie S1), demonstrating its potential applications to store intermittent sustainable energy.

4. Conclusion

In conclusion, we introduced Mo, Ru and GQDs to active inertness 1D Cu-based nanowires by surface oxidative corrosion, solvothermal and
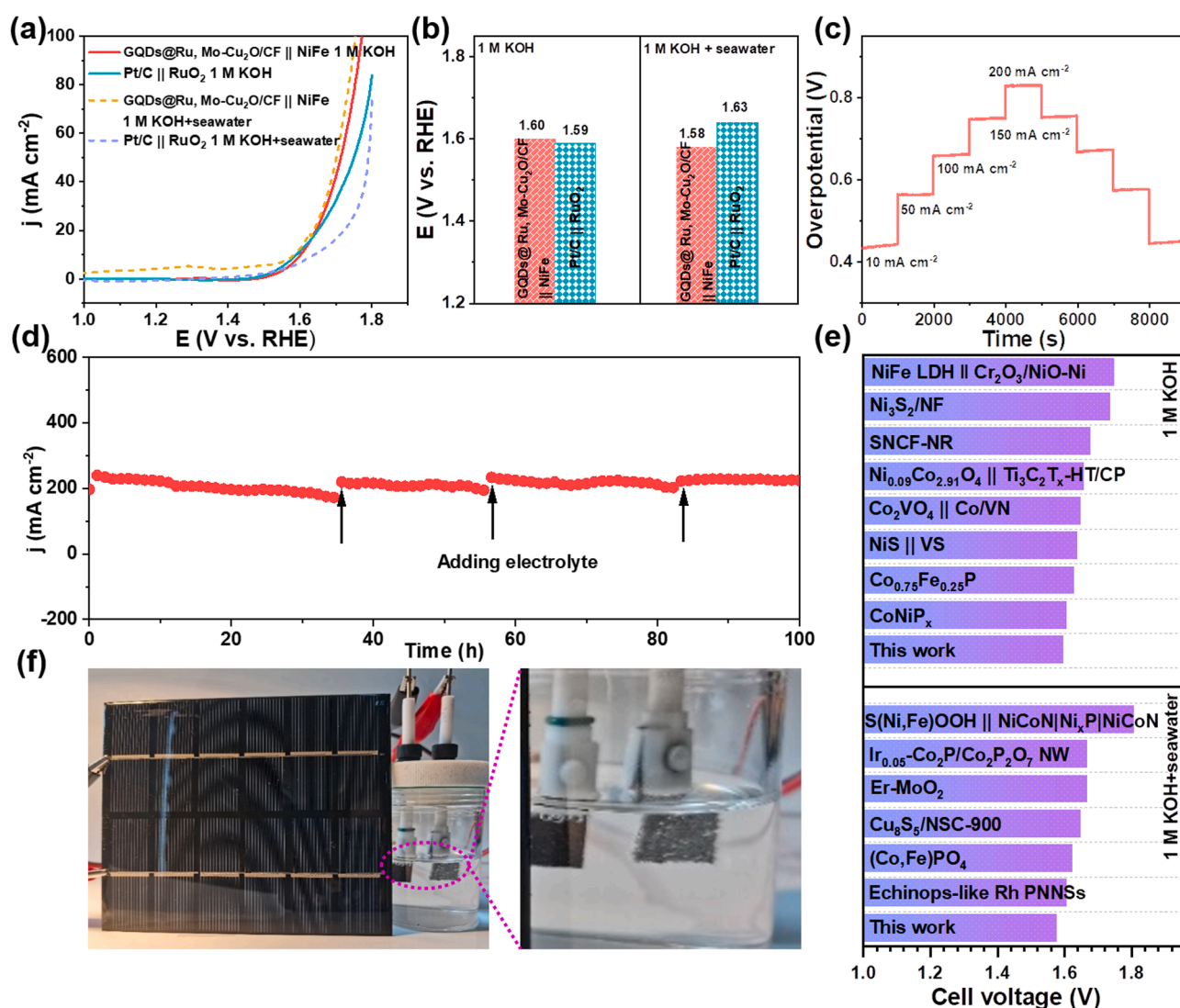
Fig. 7. (a) LSV curves of GQDs@ Ru, Mo-Cu₂O/CF || NiFe and Pt/C || RuO₂ for overall freshwater/seawater-splitting. (b) Relevant overpotentials for self-assembled electrolyzer. (c) The multi-step chronopotentiometric curve of GQDs@ Ru, Mo-Cu₂O/CF || NiFe. (d) Stability tests of GQDs@ Ru, Mo-Cu₂O/CF || NiFe in alkaline seawater. (e) Comparison of the cell voltages with reported catalysts. (f) Electrocatalytic water splitting is powered by solar energy.

low-temperature calcination approach. The designed specific 1D nanowire structure with rough surface benefits to expose enriched active sites, and favors the electrolyte transport. Importantly, the porous copper foam also accelerates the mass transport and the release of generated bubbles. The metals Mo, Ru can act as active sites to boost the water molecule dissociation and favorable hydrogen intermediate adsorption/desorption. Moreover, GQDs favors electron transport and active sites exposure. Thus, GQDs@ Ru, Mo-Cu₂O/CF exhibits superior HER performance and stability in wide pH. In particular, the self-assembled electrolyzer exhibits excellent stability at 200 mA cm⁻² for 100 h. This work provides a novel and effective method to active inert materials for efficient hydrogen production.

CRediT authorship contribution statement

Wu Zexing: Writing – review & editing. **Wang Lei:** Funding acquisition. **Wang Jinsong:** Data curation. **Xiao Weiping:** Data curation. **Li Zhenjiang:** Data curation. **Xin Liantao:** Data curation. **Jin Wei:** Data curation. **Han Linping:** Data curation. **Yang Pengfei:** Data curation. **Du Yingxue:** Writing – original draft. **Li Qichang:** Data curation.

Declaration of Competing Interest

The authors declare that they have no known competing financial interests or personal relationships that could have appeared to influence the work reported in this paper.

Data Availability

The authors do not have permission to share data.

Acknowledgements

Appendix A. Supporting information

Supplementary data associated with this article can be found in the online version at doi:10.1016/j.apcatb.2023.123617.

References

[1] V.D. Dang, T. Annadurai, A.P. Khedulkar, J.-Y. Lin, J. Adorna, W.-J. Yu, B. Pandit, T.V. Huynh, R.-A. Doong, S-scheme N-doped carbon dots anchored g-C₃N₄/Fe₂O₃ shell/core composite for photoelectrocatalytic trimethoprim degradation and water splitting, Appl. Catal. B: Environ. 320 (2023), 121928.

[2] M. Jin, R. Wang, B. Jia, J. Zhang, H. Liu, S.-Y. Lu, Achieving uniform Pt deposition site by tuning the surface microenvironment of bamboo-like carbon nanotubes, Appl. Surf. Sci. 591 (2022), 153201.

[3] T. Wang, X. Cao, L. Jiao, Ni₂P/NiMoP heterostructure as a bifunctional electrocatalyst for energy-saving hydrogen production, eScience 1 (2021) 69–74.

[4] J. Li, S. Wang, J. Chang, L. Feng, A review of Ni based powder catalyst for urea oxidation in assisting water splitting reaction,, Adv. Powder Mater. 1 (2022), 100030.

[5] Z. Zhang, K. Chen, Q. Zhao, M. Huang, X. Ouyang, Electrocatalytic and photocatalytic performance of noble metal doped monolayer MoS₂ in the hydrogen evolution reaction: a first principles study, Nano Mater. Sci. 3 (2021) 89–94.

[6] S. Xin, Y. Tang, B. Jia, Z. Zhang, C. Li, R. Bao, C. Li, J. Yi, J. Wang, T. Ma, Coupling adsorbed evolution and lattice oxygen mechanism in Fe-Co(OH)ₓ/Fe₂O₃ heterostructure for enhanced electrochemical water oxidation, Adv. Funct. Mater. 33 (2023) 2305243.

[7] X. Hu, Y. Li, X. Wei, L. Wang, H. She, J. Huang, Q. Wang, Preparation of double-layered Co−Ci/NiFeOOH co-catalyst for highly meliorated PEC performance in water splitting, Adv. Powder Mater. 1 (2022) 100024.

[8] X. Wang, H. Huang, J. Qian, Y. Li, K. Shen, Intensified Kirkendall effect assisted construction of double-shell hollow Cu-doped CoP nanoparticles anchored by carbon arrays for water splitting, Appl. Catal. B: Environ. 325 (2023), 122295.

[9] X. Guo, X. Wan, Q. Liu, Y. Li, W. Li, J. Shui, Phosphated IrMo bimetallic cluster for efficient hydrogen evolution reaction, eScience 2 (2022) 304–310.

[10] Z. Wu, P. Yang, Q. Li, W. Xiao, Z. Li, G. Xu, F. Liu, B. Jia, T. Ma, S. Feng, L. Wang, Microwave synthesis of Pt clusters on black TiO₂ with abundant oxygen vacancies for efficient acidic electrocatalytic hydrogen evolution, Angew. Chem. Int. Ed. 62 (2023), e2023004.

[11] Z. Sun, M. Yuan, H. Yang, L. Lin, H. Jiang, S. Ge, H. Li, G. Sun, S. Ma, X. Yang, 3D porous amorphous γ-CrOOH on Ni foam as bifunctional electrocatalyst for overall water splitting, Inorg. Chem. 58 (2019) 4014–4018.

[12] N. You, S. Cao, M. Huang, X. Fan, K. Shi, H. Huang, Z. Chen, Z. Yang, W. Zhang, Constructing P-CoMoO₄@NiCoP heterostructure nanoarrays on Ni foam as efficient bifunctional electrocatalysts for overall water splitting, Nano Mater. Sci. 5 (2023) 278–286.

[13] S.-Y. Lu, S. Li, M. Jin, J. Gao, Y. Zhang, Greatly boosting electrochemical hydrogen evolution reaction over Ni₃S₂ nanosheets rationally decorated by Ni₃Sn₂S₂ quantum dots, Appl. Catal. B: Environ. 267 (2020), 118675.

[14] Z. Wu, Y. Zhao, W. Xiao, Y. Fu, B. Jia, T. Ma, L. Wang, Metallic-bonded Pt−Co for atomically dispersed Pt in the Co₄N matrix as an efficient electrocatalyst for hydrogen generation, ACS Nano 16 (2022) 18038–18047.

[15] P. Li, G. Zhao, P. Cui, N. Cheng, M. Lao, X. Xu, S.X. Dou, W. Sun, Nickel single atom-decorated carbon nanosheets as multifunctional electrocatalyst supports toward efficient alkaline hydrogen evolution, Nano Energy 83 (2021), 105850.

[16] H. Wang, P. Yang, X. Sun, W. Xiao, X. Wang, M. Tian, G. Xu, Z. Li, Y. Zhang, F. Liu, L. Wang, Z. Wu, Co-Ru alloy nanoparticles decorated onto two-dimensional nitrogen doped carbon nanosheets towards hydrogen/oxygen evolution reaction and oxygen reduction reaction, J. Energy Chem. 87 (2023) 286, 29.

[17] Z. Sun, L. Lin, M. Yuan, H. Yao, Y. Deng, B. Huang, H. Li, G. Sun, J. Zhu, Mott–Schottky heterostructure induce the interfacial electron redistribution of MoS₂ for boosting pH-universal hydrogen evolution with Pt-like activity, Nano Energy 101 (2022), 107563.

[18] Y. Taji, A. Zagalskaya, I. Evazzade, S. Watzele, K.-T. Song, S. Xue, C. Schott, B. Garlyyev, V. Alexandrov, E. Gubanova, A.S. Bandarenka, Alkali metal cations change the hydrogen evolution reaction mechanisms at Pt electrodes in alkaline media, Nano Mater. Sci. (2022), https://doi.org/10.1016/j.nanoms.2022.09.003.

[19] L.Y. Zhang, T. Zeng, L. Zheng, Y. Wang, W. Yuan, M. Niu, C.X. Guo, D. Cao, C.M. Li, Epitaxial growth of Pt−Pd bimetallic heterostructures for the oxygen reduction reaction, Adv. Powder Mater. 2 (2023), 100131.

[20] D. Yang, J.-H. Yang, Y.-P. Yang, Z.-Y. Liu, High-dispersed ruthenium sites on copper phosphide/graphene for electrocatalytic hydrogen evolution in acidic and alkaline conditions, Appl. Catal. B: Environ. 326 (2023), 122402.

[21] J. Yu, Q. Cao, B. Feng, C. Li, J. Liu, J.K. Clark, J.-J. Delaunay, Insights into the efficiency and stability of Cu-based nanowires for electrocatalytic oxygen evolution, Nano Res. 11 (2018) 4323–4332.

[22] Y. Jia, F. Li, K. Fan, L. Sun, Cu-based bimetallic electrocatalysts for CO₂ reduction, Adv. Powder Mater. 1 (2022), 100012.

[23] P. Shen, B. Zhou, Z. Chen, W. Xiao, Y. Fu, J. Wan, Z. Wu, L. Wang, Ruthenium-doped 3D Cu₂O nanochains as efficient electrocatalyst towards hydrogen evolution and hydrazine oxidation, Appl. Catal. B: Environ. 325 (2023), 122305.

[24] X. Xu, K. Yang, J. She, Y. Zhai, M. Zhou, R. Deng, Z. Li, H. Cai, Self-supporting and bifunctional Cu-based electrocatalysts with porous structures as superior working electrodes for alkaline water splitting, CrystEngComm 25 (2023) 1276–1285.

[25] C. Song, Z. Zhao, X. Sun, Y. Zhou, Y. Wang, D. Wang, In Situ Growth of Ag Nanodots Decorated Cu₂O Porous Nanobelts Networks on Copper Foam for Efficient HER Electrocatalysis, Small 15 (2019) 1804268.

[26] J. Wang, B. Guo, J. Sun, Y. Zhou, C. Zhao, J. Wei, J. Guo, Cooperative hydrogen evolution reaction combining Cu₂₊₁O and Ru active sites, Appl. Catal. B: Environ. 324 (2023), 122169.

[27] M. Wang, W. Fu, L. Du, Y. Wei, P. Rao, L. Wei, X. Zhao, Y. Wang, S. Sun, Surface engineering by doping manganese into cobalt phosphide towards highly efficient bifunctional HER and OER electrocatalysis, Appl. Surf. Sci. 515 (2020), 146059.

[28] L. Zhang, Z. Liu, Q. Deng, Y. Sang, K. Dong, J. Ren, X. Qu, Nature-inspired construction of MOF@COF nanozyme with active sites in tailored microenvironment and pseudopodia-like surface for enhanced bacterial inhibition, Angew. Chem. In. Ed. 60 (2021) 3469–3474.

[29] J. Wang, Z. Zhang, H. Song, B. Zhang, J. Liu, X. Shai, L. Miao, Water dissociation kinetic-oriented design of nickel sulfides via tailored dual sites for efficient alkaline hydrogen evolution, Adv. Funct. Mater. 31 (2021) 2008578.

[30] L. Song, T. Zheng, L. Zheng, B. Lu, H. Chen, Q. He, W. Zheng, Y. Hou, J. Lian, Y. Wu, J. Chen, Z. Ye, J. Lu, Cobalt-doped basic iron phosphate as bifunctional electrocatalyst for long-life and high-power-density rechargeable zinc-air batteries, Appl. Catal. B: Environ. 300 (2022), 120712.

[31] J. Qian, J. Li, B. Xia, J. Zhang, Z. Zhang, C. Guan, D. Gao, W. Huang, Multi-stability modulating of alkaline-earth metal doped LaCoO₃ for rechargeable Zn-air batteries, Energy Storage Mater. 42 (2021) 470–476.

[32] Y. Sun, D. Li, J. Lu, Y. Zhang, J. Li, J. Liang, Synthesis of Ni-doped copper cobalt sulfide nanoparticles and its enhanced properties as an electrocatalyst for hydrogen evolution reaction, Cryst. Res. Technol. 54 (2019) 1800248.

[33] Y. Li, X. Zhang, L. Liu, H. Sheng, C. Li, L. Cao, H. Li, C. Xia, B. Dong, Ultra-low Pt doping and Pt–Ni pair sites in amorphous/crystalline interfacial electrocatalyst enable efficient alkaline hydrogen evolution, Small 19 (2023) 2300368.

[34] J. Zhang, Y. Liu, C. Sun, P. Xi, S. Peng, D. Gao, D. Xue, Accelerated hydrogen evolution reaction in CoS₂ by transition-metal doping, ACS Energy Lett. 3 (2018) 779–786.

[35] J. Tian, J. Chen, J. Liu, Q. Tian, P. Chen, Graphene quantum dot engineered nickel-cobalt phosphide as highly efficient bifunctional catalyst for overall water splitting, Nano Energy 48 (2018) 284–291.

[36] C.X. Guo, Y. Dong, H.B. Yang, C.M. Li, Graphene quantum dots as a green sensitizer to functionalize ZnO nanowire arrays on F-doped SnO₂glass for enhanced photoelectrochemical water splitting, Adv. Energy Mater. 3 (2013) 997–1003.

[37] S.-Y. Lu, J. Wang, X. Wang, W. Yang, M. Jin, L. Xu, H. Yang, X. Ge, C. Shang, Y. Chao, L. Zhou, K. Yin, J. Wang, L. Gu, Y. Cao, H. Ran, S. Guo, H. Liu, Janus-like BₓC/C quantum sheets with Z-scheme mechanism strengthen tumor photothermal-immunotherapy in NIR-II biowindow, Small Methods 6 (2022) 2101551.

[38] Y. Yan, J. Gong, J. Chen, Z. Zeng, W. Huang, K. Pu, J. Liu, P. Chen, Recent advances on graphene quantum dots: from chemistry and physics to applications, Adv. Mater. 31 (2019) 1808283.

[39] Z. Zeng, F.-X. Xiao, X. Gui, R. Wang, B. Liu, T.T. Yang Tan, Layer-by-layer assembly of nitrogen-doped graphene quantum dots monolayer decorated one-dimensional semiconductor nanoarchitectures for solar-driven water splitting, J. Mater. Chem. A 4 (2016) 16383–16393.

[40] C. Li, Q. Su, W. Wang, Z. Zhang, J. Duan, Boosting N₂ photoreduction using a ZnO@HCuₓS composite with high activity and easy recovery grown on a copper mesh, N. J. Chem. 47 (2023) 10216–10226.

[41] X. Wei, X. Wang, X. Tan, Q. An, L. Mai, Nanostructured conversion-type negative electrode materials for low-cost and high-performance sodium-ion batteries, Adv. Funct. Mater. 28 (2018) 1804458.

[42] W. Zhang, T. Xu, Z. Liu, N.-L. Wu, M. Wei, Hierarchical TiO₂₋ₓ imbedded with graphene quantum dots for high-performance lithium storage, Chem. Commun. 54 (2018) 1413–1416.

[43] Y. Jiang, X. Wang, D. Duan, C. He, J. Ma, W. Zhang, H. Liu, R. Long, Z. Li, T. Kong, X.J. Loh, L. Song, E. Ye, Y. Xiong, Structural reconstruction of Cu₂O superparticles toward electrocatalytic CO₂ reduction with high C²⁺ products selectivity, Adv. Sci. 9 (2022) 2105292.

[44] Q. Chen, X. An, Q. Liu, X. Wu, L. Xie, J. Zhang, W. Yao, M.S. Hamdy, Q. Kong, X. Sun, Boosting electrochemical nitrite–ammonia conversion properties by a Cu foam@Cu₂O catalyst, Chem. Commun. 58 (2022) 517–520.

[45] M. Nallal, K.H. Park, S. Park, J. Kim, S. Shenoy, C. Chuaicham, K. Sasaki, K. Sekar, Cu₂O/reduced graphene oxide nanocomposites for electrocatalytic overall water splitting, ACS Appl. Nano Mater. 5 (2022) 17271–17280.

[46] S. Karthikeyan, C. Chuaicham, R.R. Pawar, K. Sasaki, W. Li, A.F. Lee, K. Wilson, Template free mild hydrothermal synthesis of core–shell Cu₂O(Cu)@CuO visible light photocatalysts for N-acetyl-para-aminophenol degradation, J. Mater. Chem. A 7 (2019) 20767–20777.

[47] K. Sekar, C. Chuaicham, B. Vellaichamy, W. Li, W. Zhuang, X. Lu, B. Ohtani, K. Sasaki, Cubic Cu₂O nanoparticles decorated on TiO₂ nanofiber heterostructure as an excellent synergistic photocatalyst for H₂ production and sulfamethoxazole degradation, Appl. Catal. B: Environ. 294 (2021), 120221.

[48] H. Guan, P. Cai, X. Zhang, Y. Zhang, G. Chen, C. Dong, Cu₂O templating strategy for the synthesis of octahedral Cu₂O@Mn(OH)₂ core–shell hierarchical structures with a superior performance supercapacitor, J. Mater. Chem. A 6 (2018) 13668–13675.

[49] Y. Chen, D. Ge, J. Zhang, R. Chu, J. Zheng, C. Wu, Y. Zeng, Y. Zhang, H. Guo, Ultrafine Mo-doped SnO₂ nanostructure and derivative Mo-doped Sn/C nanofibers for high-performance lithium-ion batteries, Nanoscale 10 (2018) 17378–17387.

[50] L. Fan, H. Shen, D. Ji, Y. Xing, L. Tao, Q. Sun, S. Guo, Biaxially compressive strain in Ni/Ru core/shell nanoplates boosts Li–CO$_2$ batteries, Adv. Mater. 34 (2022) 2204134.

[51] P. Jiang, Y. Yang, R. Shi, G. Xia, J. Chen, J. Su, Q. Chen, Pt-like electrocatalytic behavior of Ru–MoO$_2$ nanocomposites for the hydrogen evolution reaction, J. Mater. Chem. A 5 (2017) 5475–5485.

[52] Y. Xue, Y. Xu, Q. Yan, K. Zhu, K. Ye, J. Yan, Q. Wang, D. Cao, G. Wang, Coupling of Ru nanoclusters decorated mixed-phase (1T and 2H) MoSe$_2$ on biomass-derived carbon substrate for advanced hydrogen evolution reaction, J. Colloid Interf. Sci. 617 (2022) 594–603.

[53] R.G. Haverkamp, An XPS study of the fluorination of carbon anodes in molten NaF–AlF$_3$–CaF$_2$, J. Mater. Sci. 47 (2011) 1262–1267.

[54] H. Chen, G. Sun, Z. Yang, T. Wang, G. Bai, J. Wang, R. Chen, S. Han, Ultra-sensitive, lightweight, and flexible composite sponges for stress sensors based combining of "through-hole" polyimide sponge and "pleated stacked" reduced graphene oxide, Compos. Sci. Technol. 218 (2022), 109179.

[55] S. Han, X. Huang, M. Fang, W. Zhao, S. Xu, D. Zhu, W. Xu, M. Fang, W. Liu, P. Cao, Y. Lu, High-performance UV detectors based on room-temperature deposited amorphous Ga$_2$O$_3$ thin films by RF magnetron sputtering, J. Mater. Chem. C. 7 (2019) 11834–11844.

[56] J. Ahire, B.M. Bhanage, Solar energy-controlled shape selective synthesis of zinc oxide nanomaterials and its catalytic application in synthesis of glycerol carbonate, J. Solid State Chem. 295 (2021), 121927.

[57] Y. Fan, X. Chen, L. Zhang, J. Wu, L. Wang, S. Yu, M. Wu, Electrochemical performance of SnO$_2$/C nanocomposites as anode materials for lithium-ion batteries, Ionics 29 (2022) 497–504.

[58] A.K. Manal, J.H. Advani, R. Srivastava, Bifunctional acid-base zirconium phosphonate for catalytic transfer hydrogenation of levulinic acid and cascade transformation of furfural to biofuel molecules, ChemCatChem 14 (2022), e202200576.

[59] S. Potgieter-Vermaak, N. Maledi, N. Wagner, J.H.P. Van Heerden, R. Van Grieken, J.H. Potgieter, Raman spectroscopy for the analysis of coal: a review, J. Raman Spectros. 42 (2011) 123–129.

[60] Q. Liu, H. Tian, J. Li, A. Hu, X. He, M. Sui, X. Guo, Hybrid graphene/Cu$_2$O quantum dot photodetectors with ultrahigh responsivity, Adv. Opt. Mater. 7 (2019) 1900455.

[61] Y. Gao, S. Yu, P. Zhou, X. Ren, Z. Wang, Z. Zheng, P. Wang, H. Cheng, Y. Liu, W. Wei, Y. Dai, B. Huang, Promoting electrocatalytic reduction of CO$_2$ to C$_2$H$_4$ production by inhibiting C$_2$H$_5$OH desorption from Cu$_2$O/C composite, Small 18 (2021) 2105212.

[62] F. Zhang, R. Zhao, Y. Wang, L. Han, J. Gu, Z. Niu, Y. Yuan, N. Qu, J. Meng, D. Wang, Superwettable surface-dependent efficiently electrocatalytic water splitting based on their excellent liquid adsorption and gas desorption, Chem. Eng. J. 452 (2023), 139513.

[63] Y. Gao, D. Zheng, Q. Li, W. Xiao, T. Ma, Y. Fu, Z. Wu, L. Wang, 3D Co$_3$O$_4$-RuO$_2$ hollow spheres with abundant interfaces as advanced trifunctional electrocatalyst for water-splitting and flexible Zn–air battery, Adv. Funct. Mater. 32 (2022) 2203206.

[64] K. Sekar, C. Chuaicham, U. Balijapalli, W. Li, K. Wilson, A.F. Lee, K. Sasaki, Surfactant- and template-free hydrothermal assembly of Cu$_2$O visible light photocatalysts for trimethoprim degradation, Appl. Catal. B: Environ. 284 (2021), 119741.

[65] J.-s Zhu, H. Yang, W. Zhang, Y. Mao, S.-s Lyu, J. Chen, An In situ Raman study of intermediate adsorption engineering by high-index facet control during the hydrogen evolution reaction, Inorg. Chem. Front. 7 (2020) 1892–1899.

[66] Q. Dai, L. Wang, K. Wang, X. Sang, Z. Li, B. Yang, J. Chen, L. Lei, L. Dai, Y. Hou, Accelerated water dissociation kinetics by electron-enriched cobalt sites for efficient alkaline hydrogen evolution, Adv. Funct. Mater. 32 (2021) 2109556.

[67] Q. Li, F. Huang, S. Li, H. Zhang, X.Y. Yu, Oxygen vacancy engineering synergistic with surface hydrophilicity modification of hollow Ru doped CoNi-LDH nanotube arrays for boosting hydrogen evolution, Small 18 (2021) 2104323.

[68] Z.-Z. Liu, X. Shang, B. Dong, Y.-M. Chai, Triple Ni-Co-Mo metal sulfides with one-dimensional and hierarchical nanostructures towards highly efficient hydrogen evolution reaction, J. Catal. 361 (2018) 204–213.